

Water jet indentation for local elasticity measurements of soft materials^{*}

N.R. Chevalier^{1,a}, Ph. Dantan¹, E. Gazquez^{2,3}, A.J.M. Cornelissen¹, and V. Fleury¹

¹ Laboratoire Matière et Systèmes Complexes, Université Paris Diderot/CNRS UMR 7057, 10 rue Alice Domon et Léonie Duquet, 75013 Paris, France

² UMR144, CNRS-Institut Curie, 26, rue d'Ulm, 75248 Paris cedex 05, France

³ Present address: INSERM U955, Equipe 6, F-94000 Créteil, France

Received 27 July 2015 and Received in final form 22 September 2015

Published online: 29 January 2016 – © EDP Sciences / Società Italiana di Fisica / Springer-Verlag 2016

Abstract. We present a novel elastography method for soft materials (100 Pa–100 kPa) based on indentation by a μm -sized water jet. We show that the jet creates a localized deformation (“cavity”) of the material that can be easily visualized. We study experimentally how cavity width and depth depend on jet speed, height, incidence angle and sample elasticity. We describe how to calibrate the indenter using gels of known stiffness. We then demonstrate that the indenter yields quantitative elasticity values within 10% of those measured by shear rheometry. We corroborate our experimental findings with fluid-solid finite-element simulations that quantitatively predict the cavity profile and fluid flow lines. The water jet indenter permits *in situ* local stiffness measurements of 2D or 3D gels used for cell culture in physiological buffer, is able to assess stiffness heterogeneities with a lateral resolution in the range 50–500 μm (at the tissue scale) and can be assembled at low cost with standard material from a biology laboratory. We therefore believe it will become a valuable method to measure the stiffness of a wide range of soft, synthetic or biological materials.

1 Introduction

Recent advances in cellular and developmental biology have put in the limelight the importance of tissue and substrate mechanical properties on differentiation, migration and morphogenesis. Engler and colleagues [1,2] demonstrated that mesenchymal stem cells differentiated preferentially to neurons, muscle or bone tissue when they are cultured on, respectively, soft, medium and high stiffness gel substrates. Durotaxis, the phenomenon by which cells tend to migrate towards stiffer areas in 2D cultures, has revealed a fundamental mechanism of cell locomotion in mechanically heterogeneous environments [3,4]. More recently, buckling along boundaries between territories of differing elasticity has been suggested as a mechanism for early vertebrate body formation [5], and further research suggests that mechanical properties play a key role in heart tissue development [6]. In the area of plant development, it has become apparent that tissue mechanical properties and stiffness gradients play key roles in plant morphogenesis [7].

All these scientific breakthroughs have relied on precise measurements of elasticity. Some of the commonly used macroscopic methods are uniaxial stretching, shear rheometry and bead indentation. These require homogeneous, centimeter sized samples. At a micron-scale, atomic force microscope (AFM) tips functionalized with μm -sized beads allow to establish stiffness maps by point-by-point sampling of indentation curves. The method is ideally suited for high resolution ($< 1 \mu\text{m}$) mapping over small sample areas (typically $100 \times 100 \mu\text{m}$ for a broad-range *XY* piezo). It is however time-consuming (typically ~ 1 s per indentation curve, *i.e.*, per pixel) and not convenient for sample sizes exceeding a few $100 \mu\text{m}$. In the latter size range several contact techniques have been proposed such as simple schemes relying on indentation with thin wires [8] techniques relying on video detection of the deflection of thin beams to measure down to μNewton forces [9], tissue aspiration inside micropipettes [10] or MEMs sensors [11]. Several acoustic methods, like the acoustic water jet [12–15] and elastography [16] also typically have a down to $\sim 100 \mu\text{m}$ size resolution. Recently, Sanchez *et al.* [17] introduced a micrometer-sized pressurized water jet indenter to measure the local elastic properties of cells. The indentation depth is measured by ionic conductance microscopy (ICM), via an ionic current established between the sample and the pipette tip. Acoustic

^{*} Supplementary material in the form of one .pdf file, one .avi file and two .mpg files are available from the Journal web page at

<http://dx.doi.org/10.1140/epje/i2016-16010-1>

^a e-mail: nicolas.chevalier@univ-paris-diderot.fr

water jet, acoustic elastography and ICM all hold great promise for stiffness mapping of biological samples but require specialized and costly equipment.

The method of stiffness determination we propose here relies on a direct optical read out of the width and depth of an indent created by a pressurized water jet. It is an extension of the air-puff tonometer that was developed by one of us [18]; both are based on the principle of tonometry, which is a well-known contactless method to measure eye pressure [19] or skin elasticity [20]. The advantages of the method we describe here are as follows:

- The system can be assembled with standard biology laboratory equipment, making it affordable and accessible for stiffness determination of typical gel substrates for cell culture like polyacrylamide, PDMS or collagen gels. It does not require any force sensor or extraneous ionic, acoustic or optical probes to read out cavity size.
- It is suited for *in situ* measurements of gels seeded with cells or tissues in 2D or 3D (embedded) as the measurement is non-invasive and exerts a pressure on a restricted area, typically 0.05 mm^2 . It is intrinsically compatible with water-based gels or tissues in physiological saline as the measurement is performed in a fully submerged state. As the probe is small, it is compatible with a wide variety of sample sizes and geometries.
- The spatial resolution of the apparatus is determined by the diameter of the pipette used. Elasticity measurements in the range from 100 Pa to 50 kPa, *i.e.*, encompassing the stiffness of most soft biological tissues, can be achieved with a standard syringe pump driving a flow through a pipette of diameter $\sim 200 \mu\text{m}$. This spatial resolution is intermediate between that of the AFM and that of macroscopic methods like tensile testing or shear rheometry, and therefore fills a gap to study stiffness heterogeneities at this spatial scale.
- As the pressure is applied by a fluid jet, it does not require approach-retract movements in the direction perpendicular to the sample as for bead-indentation (AFM). The nozzle can therefore be kept at a fixed height above the sample while the latter is displaced in the XY (in-plane) directions for stiffness mapping.

We first present the measurement setup and a brief theoretical introduction to grasp the main parameters of the instrument and their relation to indentation size. We then present detailed experimental results regarding the dependence of cavity depth on pressure, show how the indenter can be calibrated using reference polyacrylamide gels and use the calibrated indenter to measure the elastic properties of PDMS gels. We next turn to fluid-solid finite-element computations of the cavity profile and jet flow and compare them to our experimental results. We conclude by considering our results in the context of other work based on soft material local indentation, and discuss current limitations and potential upgrades and applications of the water jet indenter.

2 Results

2.1 Setup description, parameters

The setup is described in fig. 1a. The core component is a pulled glass pipette, connected via flexible silicone tubing to a syringe pump (KD Scientific Model 200, 35 lb nominal force) and a water (or physiological buffer depending on sample type) reservoir for syringe refill (50 mL). Samples are glued to the bottom of a dish filled with water. The sample dish or the pipette is secured to a Z micrometric stage that allows for precise setting of pipette-to-sample distance. An XY micrometric stage can further be used for precision XY displacements of the sample to measure in-plane stiffness variations. In this study, the samples we considered were homogeneous polyacrylamide (PAA) and polydimethylsiloxane (PDMS) gels.

The cavity can be viewed from on top using a standard binocular (Leica MZ16F). The pipette is tilted at a small angle (in this study: $\theta = 20^\circ$) and lifted a distance h from the sample surface. For relatively transparent samples, setting the illumination mirror so that the sample is illuminated in transmitted twilight (pseudo Schlieren illumination) makes the thickness variation from the indentation and the resulting cavity contour visible, as seen in the inset of fig. 1b. This does not however give access to cavity depth. It also is not clear from the on-top view whether the spot contour reflects the real physical dimensions of the cavity or whether they might include optical effects due to light refraction on the cavity profile (lens effect). To clarify these points, we additionally imaged the cavity sideways in a parallel-walled optically clear dish (cut plastic cell culture bottle) using a camera ($1600 \times 1200 \text{ px}$, Stingray) equipped with a macro-lens. The cavity can be imaged in reflected light for relatively transparent samples, even when it is located in the bulk of the gel (not at a sample edge). Relatively stiff gels ($E > 5 \text{ kPa}$) had a well-defined edge on profile views so that their width could be measured unambiguously. For these gels, simultaneous sideways (fig. 1b) and from-on-top imaging revealed that contour diameter as seen from on top is identical to the real physical width as seen from a profile view, without additional optical effects. Cavity width is almost independent of jet speed for normal incidence and equal to $\sim 1.9\varnothing$. For tilted pipettes ($\theta \neq 0$), cavity width increases as the jet speed increases. The cavity reaches a stationary shape almost instantaneously when the sample is displaced in the XY plane (Movie 1), presumably because of the almost purely elastic (non-viscous) behavior of the PAA gels.

The minimal size of the pipette that can be used (and consequently, the XY resolution of the instrument) is dictated by the maximum force that can be generated by the syringe pump as it has to overcome the $\propto \varnothing^4$ load loss within the pipette. For the standard perfusion syringe pump we used, we found that a pipette diameter $\varnothing = 200 \mu\text{m}$ was adequate to indent samples up to 50 kPa; higher jet speeds required to indent stiffer samples led to stalling of the syringe pump. Smaller pipettes (better XY resolution) and/or stiffer samples could be used by coupling to a higher-performance microfluidic syringe pumps.

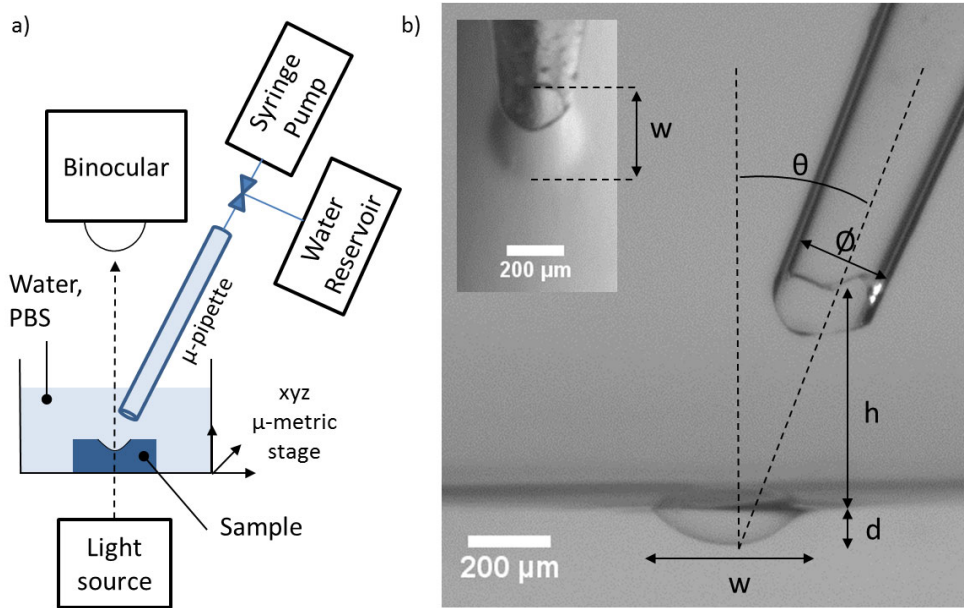


Fig. 1. a) Setup components and scheme to obtain “from-on-top” images of the cavity. b) Profile view of the cavity on a 26.5 kPa PAA gel at a jet speed of 5.15 m/s and pipette angle of 20° . Geometrical parameters of the setup include pipette diameter \varnothing , pipette-to-sample distance h , and tilt θ . The cavity is characterized by its width w and depth d . Inset: “from-on-top” view of the cavity. The mirror of the binocular is set so the sample is illuminated in twilight, which reveals thickness differences across the sample. For relatively stiff gels, which have a sharp cavity edge, the spot diameter as viewed from on top is identical to the cavity width measured from a profile view.

2.2 Basic theory

The mean velocity of the jet v is related to the volume flow Q (m^3/s , controlled by the syringe pump) by $Q = v\pi R^2$, where R is the jet radius. For normal jet incidence, the normal component of the momentum flux carried by the jet before it hits the substrate is ρvQ . Let us assume that, after the jet hits the substrate, it flows radially outward, following the substrate surface (we will justify this assumption later). The conservation of the normal component of momentum entails that the force exerted by the jet on the substrate is $F = \rho vQ$, and the pressure is $\Delta P = \frac{F}{\pi R^2} = \rho v^2$. When the jet is tilted at an angle θ , the component of the velocity normal to the surface decreases by a factor $\cos\theta$ and the area over which the jet impinges increases by a factor $1/\cos\theta$. The net pressure at the surface for a tilted pipette is therefore $\rho v^2 \cos^3\theta$. For the case of a deformable elastic substrate, it is useful to introduce a dimensionless pressure defined as the ratio of jet pressure over the elastic modulus E of the material:

$$\Delta\tilde{P} = \rho v^2 \cos^3\theta / E. \quad (1)$$

Since, as will be seen, the stress and strain are located primarily in the area of the cavity, and the width of the cavity w is determined by the diameter of the jet \varnothing (typically $1.5\varnothing < w < 3\varnothing$, see fig. 4a) we introduce the local deformation with a dimensionless prefactor $1/\alpha$ (of order ~ 1) which will be used as a fitting parameter for our experimental results

$$\varepsilon = \frac{1}{\alpha} \frac{d}{\varnothing}. \quad (2)$$

An application of Hooke’s law $\Delta\tilde{P} = \varepsilon$ then yields the following empirical relationship for the relative depth:

$$\frac{d}{\varnothing} = \alpha \Delta\tilde{P}. \quad (3)$$

This dependence of cavity depth on pipette diameter and elastic modulus is the same as found by Johnson [22] for the case of a uniform pressure applied within a disc of radius r_i to a semi-infinite elastic material.

2.3 Experimental results

Dependence of cavity size on pipette-to-sample distance

We first examined the influence of pipette-to-sample distance h on cavity width and depth (fig. 2).

As the water jet travels from the nozzle to the surface, it is slowed down by viscous forces from the surrounding resting water. At high Reynolds number, vortices are created at the jet edge. Both have the effect of enlarging the jet diameter as it propagates through the water. We have found that for high jet speeds ($v \gtrsim 3$ m/s) required to indent the harder gels, this effect is negligible and the cavity depth and width stay almost constant when varying the pipette to sample distance from $100\ \mu\text{m}$ to $2000\ \mu\text{m}$ (a similar result had been obtained for air-tonometry [17]). As the jet speed is lowered ($v \lesssim 3$ m/s), the cavity depth decreases and its width increases with increasing h . At $v = 2.3$ m/s (fig. 2), the change in cavity depth and width (relative to their respective sizes at $h = 0$) per μm of pipette-to-surface distance is respectively found to

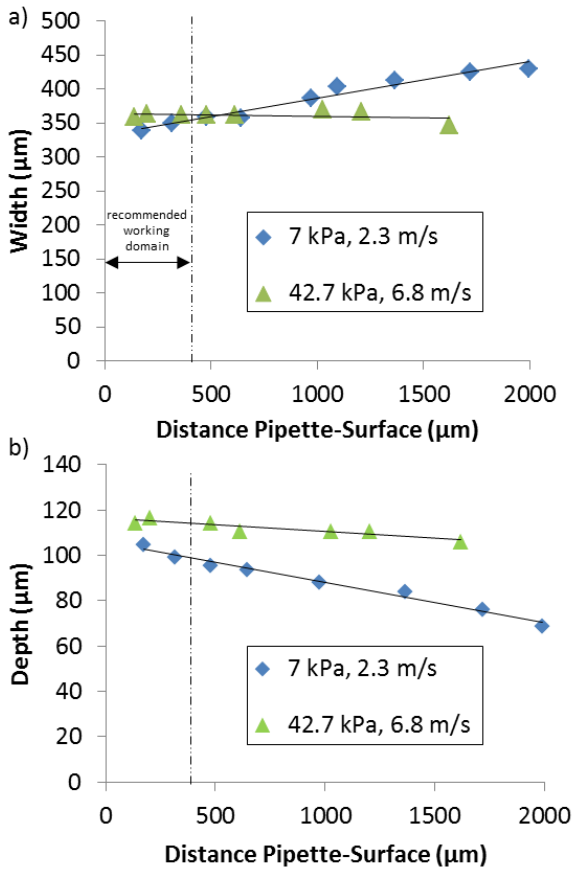


Fig. 2. Width (a) and depth (b) dependence of the cavity on pipette-to-sample distance h at normal incidence ($\theta = 0^\circ$) for a soft (7 kPa) PAA gel indented at a jet speed $v = 2.3 \text{ m/s}$ and for a hard (42.7 kPa) PAA gel indented at $v = 6.8 \text{ m/s}$. Uncertainties on cavity depth or width are smaller than symbol size. The pipette-to-sample distance h used in this work ($400 \mu\text{m}$) is indicated by a dashed line; we recommend using the indenter at small pipette-to-sample distances to minimize fluid friction effects. Straight lines are linear fits of the data.

be $-0.016\%/ \mu\text{m}$ and $+0.017\%/ \mu\text{m}$. This means that a $100 \mu\text{m}$ increase in sample-to-pipette distance (due for example to sample surface roughness) will bring about a decrease of cavity depth of 1.6% and an increase of cavity width of 1.7%. This error is well within the resolution of the measurement of cavity size, but becomes larger as smaller jet speeds (softer samples) are used. We therefore in general recommend keeping a minimal and constant distance between sample and pipette nozzle. It is further expected that friction effects will be higher for smaller pipette diameters, as the ratio of viscous friction to jet inertia increases.

Dependence of cavity depth on pressure

At dimensionless pressures $\Delta\tilde{P} < 0.4$ the cavity profile is smooth. As from $\Delta\tilde{P} \sim 0.4$, the cavity profile exhibits a sharp edge: outside of this edge, the gel is bent slightly inward towards the pipette axis; inside the edge, the gel

forms a highly curved cavity (fig. 3a,c). In Movie 1, we show how the cavity deepens as the jet speed is gradually increased. The cavity is symmetrical at normal incidence and almost symmetrical at a 20° pipette tilt at low dimensionless pressures ($\Delta\tilde{P} < 0.4$). At $\theta = 20^\circ$ and for sufficiently high $\Delta\tilde{P}$ it becomes asymmetrical as shown in fig. 3c, with the bottom of the cavity being displaced away from the pipette axis.

Cavity depth and width could be resolved with our optical system as from $\Delta\tilde{P} \sim 0.2$. Above a certain pressure, typically in the range $\Delta\tilde{P} \sim 1.2$ –2, the cavity became non-stationary: the side of the cavity most distant from the pipette exhibited an oscillatory behavior. We believe this instability to be similar to that observed for air streams through compliant nozzles [23], the cavity in the gel playing the role of the compliant nozzle. In this report, we only considered stationary cavities; a detailed study of the instability will be reported elsewhere.

In fig. 3 b and d, we measured the depth-pressure relationship of the cavity for 8 different polyacrylamide (PAA) gels of stiffness in the range 0.2–50 kPa (see gel preparation protocol in Materials and Methods) at a constant pipette-to-sample surface distance of $400 \mu\text{m}$. For the tilted pipette configuration, we measured the maximum depth (not the depth at the cavity center). The relative depth of the cavity was found to scale linearly with $\Delta\tilde{P}$, in agreement with (3). The pre-factor α was found to lie in the range 0.57–0.83 at normal incidence and in the range 0.65–0.96 for a 20° pipette tilt angle. We found no correlation between gel stiffness (or jet speed) and the value of α . The spread of α is therefore probably due to experimental uncertainty, due in particular to the difficulty of positioning the camera axis exactly parallel to the plane of the gel. Averaging over the different values of α obtained for the 8 different gels, we find $\alpha_{\text{avg},0^\circ} = 0.70 \pm 0.07$ and $\alpha_{\text{avg},20^\circ} = 0.82 \pm 0.08$. These values of α , together with eq. (3), can be used to estimate the modulus of a material from the depth of the cavity obtained at a given flow rate.

Calibration of the water jet indenter using from-on-top views of the cavity

It is difficult in many applications to obtain a profile view of the material of interest. We therefore investigated how the water jet indenter could be used to determine gel elasticities by relying merely on from-on-top views of the cavity, at a 20° pipette tilt angle. As depth is not accessible when visualizing the cavity from on top, we quantified the extent of indentation by measuring the cavity area. The principle of the measurement is to first calibrate the pipette by measuring the cavity area-volume flow dependence on a set of reference samples of known elasticity. This calibration characterizes the indenter with a single parameter. Once calibrated, the indenter can then be used to measure the elasticity of other, unknown samples.

We fitted the cavity contour (fig. 4a) with ellipses and measured the ellipse area. Each of the PAA gel had a well-defined minimal syringe pump volume flow Q as

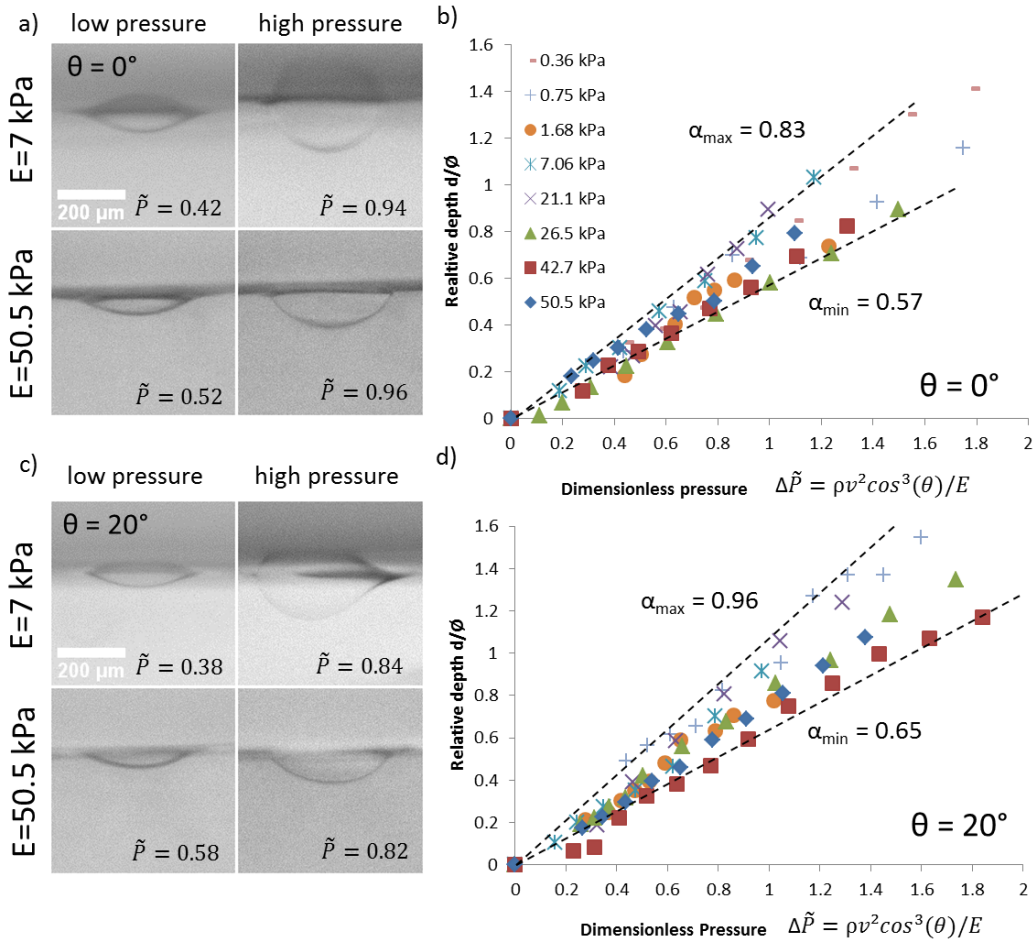


Fig. 3. Depth inferred from profile views of the cavity, $h = 400 \mu\text{m}$, $\phi = 200 \mu\text{m}$. Images of the cavity at normal (a) and 20° incidence (c) are shown for a soft (7 kPa) and a hard (50.5 kPa) gel, at low and high jet speed, the resulting $\Delta\tilde{P} = \rho v^2 \cos^3(\theta)/E$ is indicated in each picture. Relative depth (b,d) d/ϕ as a function of dimensionless pressure $\Delta\tilde{P}$ for normal (b) and $\theta = 20^\circ$ incidence (d) for 8 PAA gels of increasing stiffness (see Materials and methods). The color code in (d) is the same as in (b). For both tilted and normal incidence, the depth of the cavity is seen to scale linearly with the dimensionless pressure. The minimum and maximum values of the linear fit slopes α are indicated and plotted (dashed lines).

from which the cavity could be detected, and a maximum volume flow as from which the cavity became non-stationary (oscillatory). Between these two extremes, we found that the cavity area increased with increasing volume flow (fig. 4a-b), and the resulting data could be well fitted with a line. We used this linear regression to compute for each gel the required volume flow to create a cavity of a given target area. We used three different target areas A : 0.075 mm^2 , 0.085 mm^2 and 0.095 mm^2 (fig. 4b, dashed horizontal lines). As cavity area and depth of the indentation are linked, a target area has a corresponding target depth. Since jet speed and volume flow are proportional, $v \propto Q$, and since according to (3) cavity depth scales as $d \propto v^2/E$, we find that the required volume flow to reach a target depth (or target area) for a gel of modulus E is such that

$$E = \beta_A Q^2, \quad (4)$$

where the factor β_A (units: $\text{kPa min}^2/\text{mL}^2$) depends on the cavity target area A , jet diameter and tilt angle, but

not on the elastic properties of the sample. In fig. 4c, we experimentally find that the modulus-volume flow data can indeed be well fitted with parabolas. These fits yield β_A for the three target areas considered, they are shown in the inset of fig. 4c as a function of target cavity area. The determination of β_A concludes the calibration of the water jet indenter.

Measuring the local elasticity of gel samples using from-on-top views of the cavity

The relation (4) and the values of β_A found from the calibration with PAA gels can now be used to measure the modulus of other materials by finding the volume flow required to create a cavity of a given target area. As an example we used three PDMS gels. We refer to them as PDMS #1, #2 and #3. The elastic properties of the PDMS gels had previously been characterized by parallel plate shear rheometry. Figure 5a shows example pictures of the cavity formed on PDMS #2 at 5-7 mL/min.

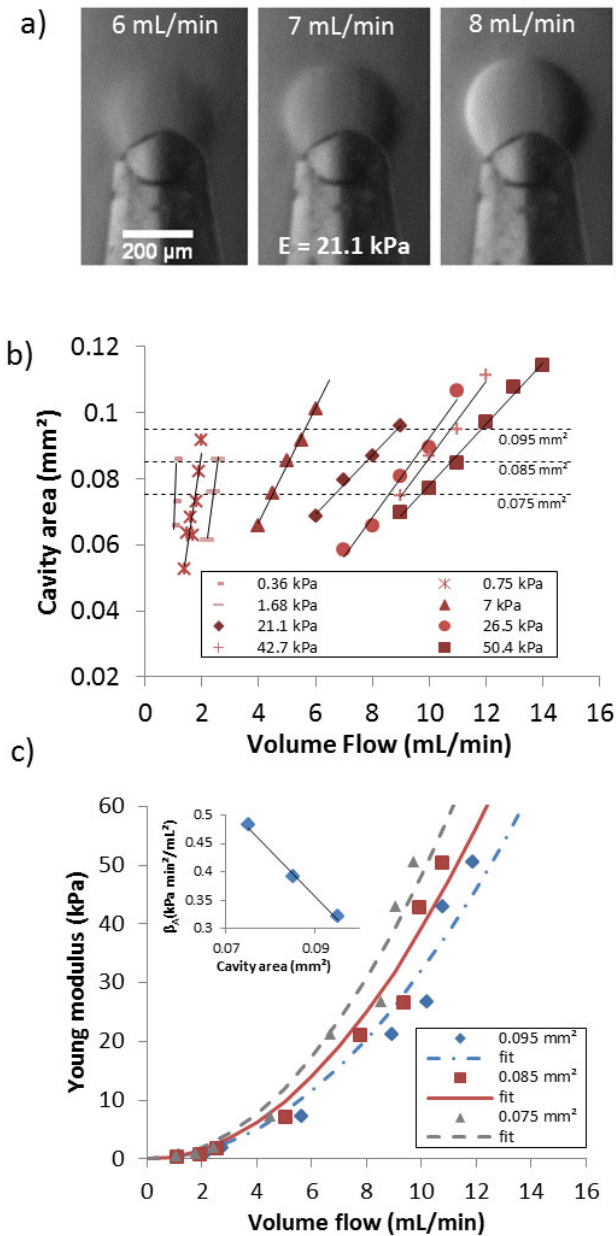


Fig. 4. Calibration of the tonometer using “from-on-top” images of the indentation on polyacrylamide gels. Pipette tilt angle $\theta = 20^\circ$, $h = 400 \mu\text{m}$, $\varnothing = 200 \mu\text{m}$. (a) View of the cavity from on top for a 21.1 kPa gel for three different volume flows, 6, 7 and 8 mL/min. The area of the cavity is deduced by fitting ellipses and measuring their area. (b) Cavity area as a function of volume flow for the 8 different PAA gels used in this study. The data for each gel was fitted with a line. The dashed horizontal lines indicate 0.075, 0.085 and 0.095 mm² target cavity areas. Error bars are smaller than symbol size. (c) Volume flow required to form a 0.075, 0.085 and 0.095 mm² cavity on each of the 8 gels used in this study, deduced from the linear regressions performed in (b). For each target area, the best parabolic fit $E = \beta_A Q^2$ is shown. Inset: parabolic fitting parameter β_A as a function of target cavity area.

To determine the elastic modulus of an unknown sample, we first measure the cavity area *versus* volume flow characteristic (fig. 5b) and determine by linear interpo-

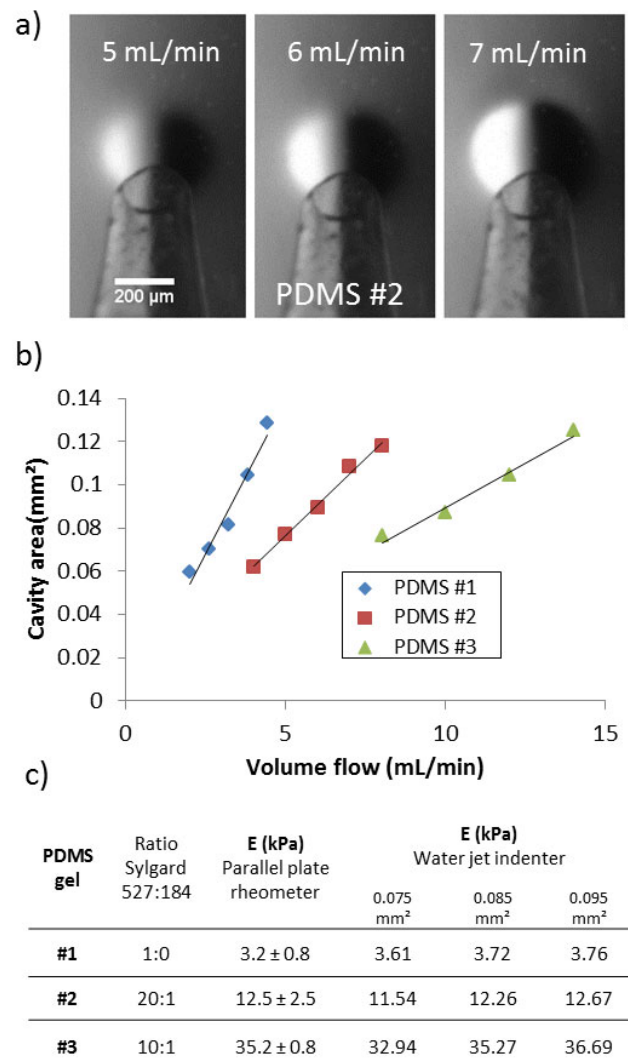


Fig. 5. Determination of the elastic modulus of PDMS gels. Pipette tilt angle $\theta = 20^\circ$, $h = 400 \mu\text{m}$, $\varnothing = 200 \mu\text{m}$. (a) Example cavity formed on PDMS #2 at 5, 6 and 7 mL/min. (b) Volume flow-cavity area dependence and linear regression for the three PDMS gels considered in this study. Error bars are smaller than symbol size. (c) Comparison of elastic modulus values measured by parallel-plate rheometry and by the water jet indenter for the three PDMS gels. Uncertainties on the values measured by rheometry are min-max values measured after 5 successive measurements. The modulus of gel #2 was inferred by interpolating values of elasticities for different PDMS 184 to 527 blend ratios (see Materials and methods section). For the water jet indenter, we list the elasticity obtained for each gel for the three different target areas 0.075, 0.085 and 0.095 mm².

lation the volume flow Q required to create a cavity of area A . The elastic modulus of the sample E is deduced from (4): $E = \beta_A Q^2$. In fig. 5c, we present the elastic modulus values obtained by this method for each of the three target areas 0.075, 0.085 and 0.095 mm², and compare these results to the elasticity measured with shear rheometry. Variations of measured elasticity with target

area are very small (at most 6%), which is consistent with the idea that the arbitrary choice of a target area should not have any influence on the outcome of the measurement. Maximum deviations of the elasticity values measured with the water jet indenter from those measured with shear-rheometry are, respectively, 13%, 8% and 6.3% for PDMS #1, #2 and #3. We believe these results confirm that the water jet indenter can be used as a reliable tool to determine the elastic modulus of soft materials.

The water jet indenter has several advantages over other methods such as shear rheometry. It does not require molding the sample in a particular shape: any sufficiently thick (~ 10 times the probe diameter) slab of material can be mounted to a Petri dish bottom and the cavity area-volume flow curves can be retrieved within minutes. As the elasticity is probed locally, measurements can be performed at different locations to probe sample stiffness heterogeneities. Finally, it is possible to set a constant jet speed and monitor variations in cavity area as the sample is displaced in the XY plane. As the jet speed (equivalently: volume flow) is kept constant, a well-defined cavity (visible and not unstable) will only be formed within a certain range of stiffness. At 6 mL/min for example (fig. 4b), a soft spot of elasticity 7 kPa would yield a close to 0.1 mm^2 cavity area whereas a stiffer spot of 21.1 kPa would yield a smaller cavity area of about 0.065 mm^2 . We experimentally found that β_A decreases linearly with increasing cavity area (fig. 4c inset). According to (4), this means that, for a constant volume flow, the elastic modulus decreases linearly with increasing cavity area. When performing water jet indentation in this “constant speed” mode, it is important to ensure flatness of the sample as variations in pipette-to-sample distance h could cause cavity area changes, especially for soft samples, when low jet speeds are used (fig. 2).

2.4 Finite-element simulation

We modeled the formation of the cavity by an impinging fluid jet using coupled fluid-solid finite-element simulations (see Materials and methods section). We were interested in knowing whether the experimental cavity profile and depth could be predicted by simulation, and to visualize flow lines and vortices resulting from the coupled interaction of the fluid with a deformable substrate.

Convergence of the computation up to deformations comparable to those measured experimentally could only be obtained by considering the gel as a hyper-elastic material. We considered the Yeoh strain energy density function, which has previously been used to model the aspiration of PAA gels in micron-sized pipettes [24]. In the Yeoh model, the non-linearity of the material at high strains is described by a single parameter, a_3 (see Materials and methods section). As we did not measure the high-strain mechanical behavior of the gels, we only compare the depth of the cavity at low pressures (low strains), where the computed depth of the cavity depends only weakly on a_3 .

Figure 6a shows that the simulation can predict cavity depth with good accuracy; the pressure-depth trend is found to be almost linear for low a_3 (*i.e.*, close to linear elastic material). The simulated cavity profiles matched closely the experimental profiles, as shown in fig. 6b. We recover the general aspect of the cavity described in the experimental part, *i.e.*, a well-defined edge (white arrow), outside of which the gel is slightly bent towards the pipette axis, and inside of which the gel forms a deep cavity of size commensurate with pipette diameter. Strain was maximal at the cavity bottom and reached about ~ 0.4 for flow velocities close to the threshold of instability.

Movie 3 shows how the flow and gel profile evolve from zero jet speed up to a fully developed cavity. As the cavity deepens, it focuses the flow, causing it to deepen more: this non-linear amplification mechanism [25] gives rise to a cavity with sharp edges. Figure 7 shows the simulated flow lines for normal (fig. 7a,b) and 20° incidence (fig. 7c). At 0° incidence, as the flow is ejected from the sides of the cavity, it is attracted back to the gel surface by a Coanda-type effect [26]. The flow outside the cavity flows radially outward, along the gel surface, just as for a water jet impacting on a solid, non-deformable surface in air. This justifies the assumptions made to derive (1), *i.e.*, the initial normal component of the momentum flux of the jet changes from $F = \rho v Q$ before it hits the surface to 0 after it has hit the surface. When the pipette is tilted, the cavity becomes slightly asymmetric, the edge most distant from the pipette becoming sharper, just as seen in the experiment (fig. 3d). Figure 7c additionally shows that the flow exiting the cavity is not attached to the gel surface as was found for normal incidence and that a vortex forms at the cavity edge located closest to the pipette.

3 Discussion

The deformation of a semi-infinite elastic material submitted to a uniform pressure ΔP inside a disc of radius r_i at the material's interface has been derived by Johnson [22], he found the following vertical displacements (cavity profile) for $r < r_i$:

$$h(r) = \frac{4(1-\nu^2)r_i\Delta P}{\pi E} E(r/r_i), \quad (5)$$

where ν is the Poisson ratio, E the elastic modulus, and $E(r/r_i)$ the complete elliptic integral of the second kind evaluated at r/r_i . The maximal displacement at the center of the disc is

$$h(r=0) = 2(1-\nu^2)r_i\Delta P/E. \quad (6)$$

It is interesting to compare this expression with our experimental results. We first notice that (6) has the same functional form as (3). If we take $r_i = R$ (the radius of the pipette) and identify $\Delta P/E$ in (6) with the dimensionless jet pressure $\Delta \tilde{P}$ given by (1), the pre-factor α introduced in (2) can be identified in the case studied by Johnson *et al.* as $\alpha_J = 1 - \nu^2$. For an incompressible material this yields $\alpha_J = 0.75$. We experimentally

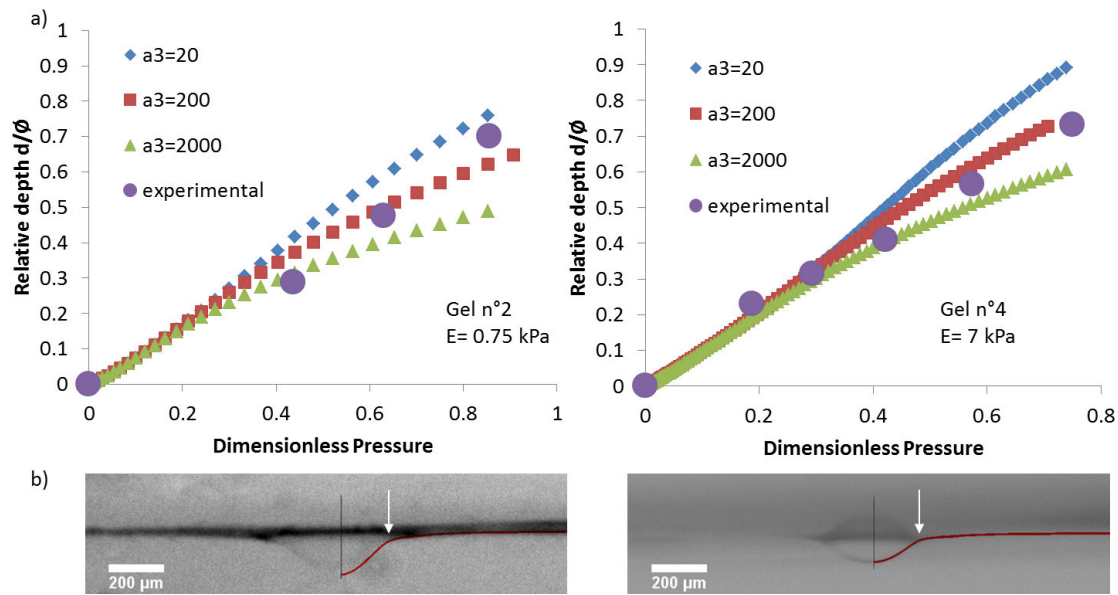


Fig. 6. Comparison of computed and experimental depth and cavity profile at 0° incidence. a) Simulation and experimental parameters: $h = 400 \mu\text{m}$, $\varnothing = 200 \mu\text{m}$, $E = 750 \text{ Pa}$ (left) or $E = 700 \text{ Pa}$ (right). For the simulation, three different values of a_3 were considered, 20, 200, 2000. At small dimensionless pressures, the cavity relative depth *vs.* dimensionless pressure curve is independent of a_3 . b) Comparison of the experimental (picture) and computed (red line) cavity profile for $E = 750 \text{ Pa}$, $v = 0.8 \text{ m/s}$, $a_3 = 20$ (left) and $E = 7060 \text{ Pa}$, $v = 2 \text{ m/s}$, $a_3 = 2000$ (right). The elasticity and speed values considered to obtain the computed profile are the same as in the experiment. The white arrow shows the cavity edge.

found $\alpha_{\text{avg},0^\circ} = 0.70 \mp 0.07$ for normal incidence and $\alpha_{\text{avg},20^\circ} = 0.82 \mp 0.08$ at a 20° tilt. The depth of the cavity can therefore be well estimated by using (6). This is not obvious as Johnson's computation assumes a uniform pressure with a sharp cut-off, whereas the real pressure profile has a bell shape. In their work on the use of the ionic scanning microscope coupled to a water jet indenter, Sanchez *et al.* [17] relied on Johnson's formula (6) to infer the relation between cavity depth and elastic modulus, as they did not have access to the indentation profile. Our work justifies both experimentally (fig. 3) and by using simulation (fig. 6) the use of this formula to infer cavity depth. We however caution that the full analytical profile (5) yields a cavity with a pointy bottom, as the elliptic integral $E(r/r_i)$ has a non-zero slope at $r = 0$. It does not reflect the actual smooth cavity profile we found by experiment and simulation.

When the pipette is tilted, it is straightforward to obtain from-on-top images of the cavity and to quantify the indentation area. We have shown that in this configuration the indentation area increases linearly with increasing jet speed. Taking advantage of this behavior, we have shown how the water jet indenter can be calibrated by measuring the required volume flow to achieve a target cavity area on a set of reference gels of known elasticity. A sufficient number of gels (8 in this work) spanning the elasticity range of interest should be used to yield a precise calibration. We have then used the calibrated indenter to measure the elasticity of soft PDMS samples and have shown that the stiffness measured by water jet indentation was within $\sim 10\%$ of that measured by shear rheometry. PDMS and PAA gels have Young elastic moduli in the range of soft bi-

ological tissues (0.2 to 50 kPa) and are commonly used as cell culture substrates for mechanobiological studies [1–4]. As substrate elasticity has been found to have a profound influence on cell behavior and as the production of gels with reproducible elastic modulus values is challenging, it is of great interest to be able to measure the local stiffness of such samples prior and during their use in cell culture.

We have finally presented how sample stiffness heterogeneities can be assessed by keeping a constant water jet speed and sample-to-pipette distance while the sample is raster scanned in the XY direction. We found this “constant speed” mode to be successful at detecting and quantifying stiffness gradients in inhomogeneous gels prepared by apposition of agarose solutions of different concentration. Image processing can be used to automatically extract the cavity area at each XY position of the sample and output stiffness maps. While it is important to ensure sample horizontality and flatness, we do not feel it is necessary at this pipette scale ($200 \mu\text{m}$) to implement a feedback loop to ensure a constant pipette-to-sample distance, as done in [17]. As the pipette we use has a ~ 200 times higher diameter than that used in the work of Sanchez *et al.* [17], slowing down of the jet by fluid-fluid friction, while still present (fig. 2), is not as critical.

Current limitations of the method we present concern mainly the sample optical properties: it must be transparent enough so that the cavity can be seen in transmitted twilight. We have not been able to detect the cavity by reflected or transmitted light on opaque, albeit smoothly cut biological samples. Reducing sample thickness is not an option as the water jet indenter requires the sample to be thicker than typical cavity depth (which is \sim pipette

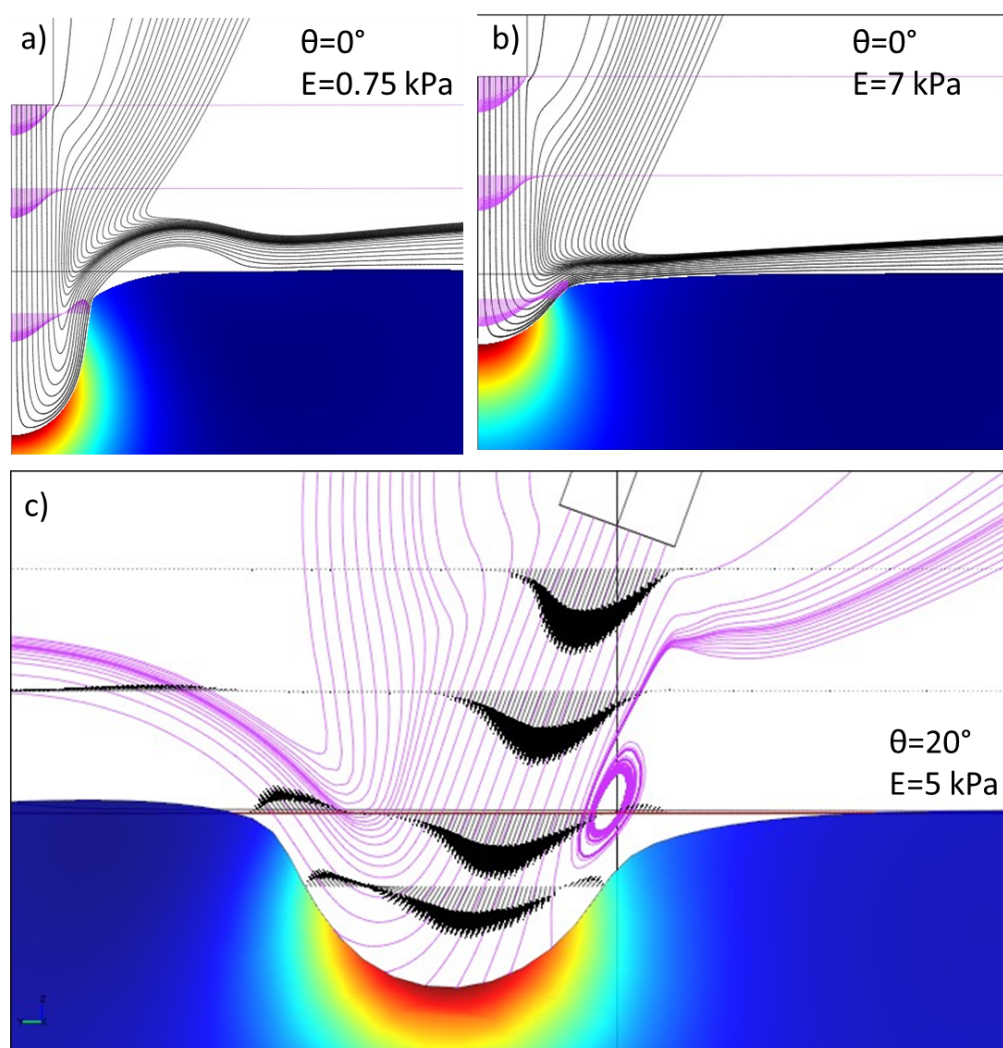


Fig. 7. Hydrodynamic flow lines, speed magnitude cross sections and gel displacement (blue to red color code in gel) for $h = 400 \mu\text{m}$, $\varnothing = 200 \mu\text{m}$ and a) $\theta = 0^\circ$, $E = 750 \text{ Pa}$, $a_3 = 20 \text{ Pa}$, $v = 1.8 \text{ m/s}$, b) $\theta = 0^\circ$, $E = 7000 \text{ Pa}$, $a_3 = 2000 \text{ Pa}$, $v = 2.575 \text{ m/s}$ and c) $\theta = 20^\circ$, $E = 5000 \text{ Pa}$, $a_3 = 2000 \text{ Pa}$, $v = 3.05 \text{ m/s}$.

diameter). Three approaches could circumvent this issue: 1°) coating the sample with a thin film or small particles of contrasting optical index material that would allow cavity visualization in reflected light without modifying sample material properties, 2°) making the biological sample transparent by decellularization [27] or by using optical clearing agents [28], 3°) using more sophisticated optical (laser reflection, see [18]), electrical [17] or acoustic methods [14] to measure cavity depth or width.

We believe that the current, accessible and easy-to-build implementation of this water jet indenter will make it a method of choice to measure *in situ* the stiffness of gels used in cell and tissue culture for biophysical and bioengineering studies.

4 Materials and methods

4.1 Pipette and syringe pump

Pipette were pulled manually by heating glass Pasteur pipette and cutting them with a silicon carbide blade to

obtain a nozzle diameter of $\sim 200 \mu\text{m}$. The diameter of the water jet (hydrodynamic diameter of the pipette) was measured in air; irregularities at the nozzle of the pipette (seen in fig. 1) did not affect the direction or cylindrical shape of the jet. The volume flow was independently measured by recording the mass of water ejected during a fixed time interval; values were equal to those indicated by the syringe pump to within 5%. Jet speeds used were in the range 0.4–9.7 m/s.

4.2 Polyacrylamide (PAA) and polydimethylsiloxane (PDMS) gel fabrication

PAA gels with stiffnesses ranging from 0.2 kPa to 50 kPa were fabricated from mixtures of acrylamide and bis-acrylamide according to the protocol of Tse & Engler [18]. The liquid PAA + PAA-bis mixture was poured in a parallel walled glass cell and left to polymerize at ambient conditions for at least 1 hour. After removal from the mould, this procedure yielded $10 \times 10 \text{ cm}$, 1.5–2 mm thick

Table 1. Properties of the PAA gels used in this study. The measured modulus is the bulk elastic modulus measured by tensile testing as described below. The mean deviation of measured E was less than 4% for the soft gel and less than 1% for the stiffer ones. Measurements were performed just prior to water jet indentation testing, but 6 months after fabrication of the gels.

Gel n°	1	2	3	4	5	6	7	8
Acrylamide (%)	3	3	4	5	10	8	8	10
Bis-Acrylamide (%)	0.06	0.1	0.1	0.15	0.1	0.264	0.48	0.26
Measured E (kPa)	0.36	0.75	1.68	7.06	21.17	26.50	42.66	50.53

square sheets of gel. This thickness is an order of magnitude higher than the maximum jet indentation depth, so that bulk compression effects of the gel from jet indentation are negligible. These sheets were kept all the time hydrated in DI water at 4 °C. For uniaxial traction tests, the sheets were further cut with a metal blade to $\sim 1.5 \times 4$ cm strips. Properties of the gels are summarized in table 1.

Soft PDMS gels were fabricated by blending Sylgard 527 and Sylgard 184 oil according to the procedure described in [29]. Sylgard 527 was mixed with its reticulant at a 1:1 ratio, yielding substance A. Sylgard 184 was mixed with its reticulant at a 10:1 ratio, yielding substance B. Substance A and B were then blended at three different ratios, 1:0, 20:1 and 10:1, to respectively yield the three different gels we used in this study, PDMS #1, #2 and #3. The blends were poured in separate Petri dishes and cured at 65 °C for 5 hours.

4.3 Gel elastic modulus determination

Stiffness of the PAA gel strips were independently measured by uniaxial tensile testing, the setup is shown in Figure S1. One end of the strip is weighted with a miniature vise whose sharp edges were wrapped with Parafilm to prevent fracture of the gel strips. The gel+vise sinks to the bottom of a square container filled with water, while the gel strip remains vertical due to buoyancy. The free end of the strip is then fastened to a paper clip. The paper clip is also submerged and attached via a thin nylon thread to a balance with 10 mg precision. The gel was stretched by displacing the container in the z -direction with a micrometric stage. During stretching, only the nylon thread is displaced out of the water, so that buoyancy changes are negligible. Ten displacement-tension points in the range 0-10 g (up to $\sim 10\%$ strain) were recorded, yielding a linear response, the measurement was repeated twice for each gel, and the slope $F/\Delta l$ was extracted. The thickness of the gels e was subsequently measured by direct profile imaging with a Stingray camera, and the width w and length l comprised between vise and clip measured with a ruler. The elastic modulus was deduced from $E = Fl/(\Delta l ew)$. The measured elastic modulus values are summarized in table 1. These calibrated gel strips were then glued with Vetbond glue to the bottom of a dish and used for water jet indentation measurements within the next 1-3 days.

Stiffness of the PDMS gels was assessed by shear rheometry after *in situ* curing of the gel at 65 °C. A maximal strain of 1% was used at 1 Hz (MCR 301, Anton Paar,

sample thickness ~ 1 mm). We convert shear modulus to Young modulus assuming a Poisson ratio $\nu = 0.5$. The elasticity of PDMS #2 was inferred from an interpolation of the experimental curve of elasticity as a function of blend ratio of Sylgard 527 to Sylgard 184 (Figure S2).

4.4 Finite elements

A fluid-structure interaction model based on the finite-element method was developed with the help of the commercial code Comsol Multiphysics. The geometry of the model consists of two adjacent coaxial cylindrical parts: a fluid (water, density $\rho = 1000$ kg/m³, dynamic viscosity $\eta = 0.001$ Pa · s) domain solved with the Navier-Stokes equations and a solid domain modeling the elastic sample governed by structural mechanics equations. Each cylinder is 6 mm diameter and 1 mm high, large enough to avoid any influence of far boundaries upon local interfacial deformation. The fluid exerts viscous and pressure forces on the solid domain, while the resulting deformation of the solid affects the geometry of the fluid domain and the flow field. Coupling is obtained by the arbitrary Lagrangian-Eulerian (ALE) method, *i.e.*, a moving mesh follows the interface displacement computed by the structural mechanics. At a 20° pipette angle, a 3-dimensional geometry is needed; at normal incidence the geometry becomes axisymmetric and can therefore be reduced to a 2-dimensional problem. The flow at the pipette outlet is assumed to be laminar with a parabolic velocity profile. For this flow, the maximal on-axis flow speed v_{\max} is twice the cross-section averaged (mean) flow speed v , *i.e.*, $v_{\max} = 2v$. At the interface, two boundary conditions have to be implemented: a kinematic condition which states that the fluid velocity is equal to the velocity of the interface (no-slip condition) and a dynamic condition about the load experienced by the sample given by: $\mathbf{F}_T = -\mathbf{n} \cdot (p\mathbf{I} + \eta(\nabla\mathbf{u} + (\nabla\mathbf{u})^T))$, where \mathbf{n} is the normal vector to the interface, p the pressure and \mathbf{u} the fluid velocity. The gel is modeled as a nonlinear hyper-elastic material defined by its strain energy function W , which is a function of the strain state. For an isotropic material, W is a function of the invariants of the right Cauchy-Green tensor \mathbf{C} : $W = W(I_1, I_2, I_3)$, where $I_1 = \text{tr}(\mathbf{C})$; $I_2 = [I_1^2 - \text{tr}(\mathbf{C}^2)]/2$; $I_3 = \det(\mathbf{C}) = J^2$. We used the stress-strain relationship derived from Yeoh's strain energy density function: $W = a_1(J^{-2/3}I_1 - 3) + k \cdot a_1(J - 1)^2 + a_3(J^{-2/3}I_1 - 3)^3$, with $k = 2(1 + \nu)/(3(1 - 2\nu))$, where $a_1 = E/6$ with E the Young modulus at low deformation, ν Poisson's ratio

taken to be 0.48 for the PAA gels and a_3 an adjustable material constant. A parametric stationary solver was used, the parameter being the velocity v_{\max} ; the computational process begins by calculating a steady solution for a small value of the parameter such that the solution can easily be computed. The flow velocity is then increased step by step, giving the nonlinear solver a good initial guess based on the solution from the previous velocity value. The computation is halted when it stops converging.

5 Supplementary material

- Supplementary information: picture of tensile test setup for gels and PDMS elastic modulus interpolation
- Movie 1: 21.1 kPa gel, increasing volume flow from 4 to 8.5 mL/min. At 8.5 mL/min, the cavity becomes blurry as it is oscillating.
- Movie 2: the cavity forms instantly as the sample is moved in the Y direction. Towards the end of the movie, an impurity impedes proper visualization of the cavity. 26.5 kPa gel, 8 mL/min.
- Movie 3: Simulation speed ramp. $E = 750$ Pa gel, $a_3 = 200$ Pa, $h = 400$ μm , $\varnothing = 200$ μm , flow speed from 0 to 2.275 m/s.

Author contribution statement

NRC and VF designed research; NRC, VF, EG and AJMC performed research; PhD performed numerical simulations; NRC wrote the paper. The authors declare no conflict of interest.

This work was funded by ANR-12-BSV2-0019, ENSINTED and by the Labex “Who Am I?”. EG was supported by a PhD fellowship from the Ministère de l’Enseignement et de la Recherche. We thank Matthieu Roché and Menghua Zhao for providing and characterizing PDMS samples.

References

1. A.J. Engler, S. Sen, H.L. Sweeney, D.E. Discher, *Cell* **126**, 677 (2006).
2. J.R. Tse, A.J. Engler, *PLoS One* **6**, e15978 (2011).
3. C.-M. Lo, H.-B. Wang, M. Dembo, Y. Wang, *Biophys. J.* **79**, 144 (2000).
4. L.G. Vincent, Y.S. Choi, B. Alonso-Latorre, J.C. del Alamo, A.J. Engler, *Biotechnol. J.* **8**, 472 (2013).
5. V. Fleury, N.R. Chevalier, F. Furfaro, J.-L. Duband, *Eur. Phys. J. E* **38**, 6 (2015).
6. S. Majkut, T. Idema, J. Swift, C. Krieger, A. Liu, D.E. Discher, *Curr. Biol.* **23**, 2434 (2013).
7. A. Peaucelle, S.A. Braybrook, L. Le Guillou, E. Bron, C. Kuhlemeier, H. Hofte, *Curr. Biol.* **21**, 1720 (2011).
8. I. Levental, K.R. Levental, E.A. Klein, R. Assoian, R.T. Miller, R.G. Wells, P.A. Janmey, *J. Phys.: Condens. Matter* **22**, 194120 (2010).
9. L. Davidson, R. Keller, *Methods Cell Biol.* **83**, 425 (2007).
10. K. Guevorkian, M.-J. Colbert, M. Durth, S. Dufour, F. Brochard-Wyart, *Phys. Rev. Lett.* **104**, 218101 (2010).
11. E.A. Corbin, L.J. Millet, J.H. Pikul, C.L. Johnson, J.G. Georgiadis, W.P. King, R. Bashir, *Biomed. Microdev.* **15**, 311 (2013).
12. S. Li, K.D. Mohan, W.W. Sanders, A.L. Oldenburg, *J. Biomed. Opt.* **16**, 116005 (2011).
13. Y.P. Zheng, M.H. Lu, Q. Wang, *Ultrasonics* **44**, 203 (2006).
14. M. Lu, Y. Zheng, Q. Huang, *Conf. Proc. IEEE Eng. Med. Biol. Soc.* **1**, 993 (2005).
15. Y. Wang, Y.P. Huang, A. Liu, W. Wan, Y.P. Zheng, *Ultrason. Med. Biol.* **40**, 1296 (2014).
16. J.L. Gennisson, T. Deffieux, M. Fink, M. Tanter, *Diag. Interv. Im.* **94**, 487 (2013).
17. D. Sánchez, N. Johnson, C. Li, P. Novak, J. Rheinlaender, Y. Zhang, U. Anand, P. Anand, J. Gorelik, G.I. Frolenkov, C. Benham, M. Lab, V.P. Ostanin, T.E. Schäffer, D. Klennerman, Y.E. Korchev, *Biophys. J.* **95**, 3017 (2008).
18. V. Fleury, A. Al-Kilani, O.P. Boryskina, A.J.M. Cornelissen, T.H. Nguyen, M. Unbekandt, L. Leroy, G. Baffet, F. Le Noble, O. Sire, E. Lahaye, V. Burgaud, *Phys. Rev. E* **81**, 1 (2010).
19. W.L. Ottar, *Insight* **23**, 11 (1998).
20. G. Boyer, C. Pailler Mattei, J. Molimard, M. Pericoi, S. Laquieze, H. Zahouani, *Med. Eng. Phys.* **34**, 172 (2012).
21. D.C. Lin, D.I. Shreiber, E.K. Dimitriadis, F. Horkay, *Biomech. Model. Mechanobiol.* **8**, 345 (2009).
22. K.L. Johnson, *Contact Mechanics* (Cambridge University Press, 1985).
23. P. Zimoch, E. Tixier, J. Hsu, A. Winter, A. Hosoi, *Fast, large amplitude vibrations of compliant cylindrical shells carrying a fluid*, ArXiv e-prints, October 2012.
24. T. Boudou, J. Ohayon, C. Picart, R.I. Pettigrew, P. Tracqui, *Biorheology* **46**, 191 (2009).
25. T. Uth, V.S. Deshpande, *Proc. Natl. Acad. Sci. U.S.A.* **110**, 20028 (2013).
26. E. Guyon, J.-P. Hulin, *Hydrodynamique Physique* (EDP Science, 2001).
27. J. Guyette, S.E. Gilpin, J.M. Charest, L.F. Tapias, X. Ren, H.C. Ott, *Perfus. Decellulariz. Whole Organs* **9**, 1451 (2014).
28. M.-T. Ke, S. Fujimoto, T. Imai, *Nat. Neurosci.* **16**, 1154 (2013).
29. R.N. Palchesko, L. Zhang, Y. Sun, A.W. Feinberg, *PLoS One* **7**, e51499 (2012) doi:10.1371/journal.pone.0051499.